Research Article

Humaira Yasmin*, Showkat Ahmad Lone, Ali M. Mahnashi, Waleed Hamali, Zehba Raizah, and Anwar Saeed*

The electrically conducting water-based nanofluid flow containing titanium and aluminum alloys over a rotating disk surface with nonlinear thermal radiation: A numerical analysis

https://doi.org/10.1515/phys-2023-0184
received October 27, 2023; accepted January 05, 2024

Abstract: A metallic alloy is a combination of two or more elements, often called a compound or a solution. Steel is largely composed of carbon, a nonmetal, but alloys are often made up of metals. In this article, the authors have explored the electrically conducting water-based viscous nanofluids flow past a rotating disk surface. The nanofluids flow is composed of titanium and aluminum alloys where water is used as a base fluid. Two important cases, namely the stretching case and the shrinking case, were investigated to analyze the flow behaviors due to the different embedding factors. The impacts of viscous Joule heating, thermophoresis, Brownian motion, activation energy, nonlinear thermal radiation, and chemical reaction are investigated here. By employing an appropriate set of variables for shifting the leading equations to dimension-free form. The mathematical model is solved numerically by incorporating the bvp4c MATLAB scheme. Current work is validated with previous studies. The outcomes showed that the radial velocity increases when the disk surface stretches and reduces when the disk surface shrinks. On the other hand, the Azimuthal velocity increases when the disk surface shrinks and reduces when disk surface stretches. Both the radial and Azimuthal velocities are the diminishing functions of the magnetic factor, whereas temperature is the growing function of magnetic factor. In addition, the temperature is more influenced by the magnetic factor in the case of nonlinear radiation. The higher magnetic factor increases skin friction. In addition, the stretching case experiences more surface drag than the shrinking case. It is found that nanofluid flow containing titanium alloy has perceived the greater impacts of the embedded factors compared to the nanofluid flow containing aluminum alloy.

Keywords: nanofluids, water, titanium and aluminum alloys, Joule heating, viscous dissipation, rotating disk, stretching/shrinking cases

*** Corresponding author: Humaira Yasmin**, Department of Basic Sciences, General Administration of the Preparatory Year, King Faisal University, 31982, Al Ahsa, Saudi Arabia, e-mail: hhassain@kfu.edu.sa
*** Corresponding author: Anwar Saeed**, Department of Mathematics, Abdul Wali Khan University, Mardan, 23200, Khyber Pakhtunkhwa, Pakistan, e-mail: anwarsaeed769@gmail.com
Showkat Ahmad Lone: Department of Basic Sciences, College of Science and Theoretical Studies, Saudi Electronic University, Jeddah-M, Riyadh 11673, Kingdom of Saudi Arabia
Ali M. Mahnashi, Waleed Hamali: Department of Mathematics, College of Science, Jazan University, Jazan, Saudi Arabia
Zehba Raizah: Department of Mathematics, College of Science, King Khalid University, Abha, Saudi Arabia

Nomenclature

u, v, w	components of flow
r, φ, z	coordinates
B_0	strength of the magnetic field
Ω	angular velocity
$u_w = ar$	stretching velocity
S	stretching/shrinking factor
$v_w = r\Omega$	rotational velocity
T	temperature
T_f	reference temperature
C	concentration
C_f	reference concentration
a	constant
ρ	density
μ	viscosity
σ, k	electrical and thermal conductivities
p	pressure
C_p	specific heat

D_B	Brownian diffusivity coefficient
D_T	thermophoretic coefficient
k_r	reaction coefficient
E_a	coefficient of activation energy
n	power index
h_f, h_c	heat and mass transfer coefficients
ϕ	nanoparticle volume fraction
M	magnetic factor
Pr	Prandtl number
ω	temperature difference factor
Bi_T, Bi_C	thermal and concentration Biot numbers
K_r	chemical reaction factor
Nt	thermophoretic factor
Rd	thermal radiation factor
Nb	Brownian motion factor
E	activation energy factor
Sc	Schmidt number
θ_w	temperature ratio factor

1 Introduction

It is difficult to achieve high competence in thermal-mass fluidity while working with ordinary fluids that have subpar thermophysical properties. The introduction of the idea of nanofluids brought the issue to some actuality. A fluid that has been infused with quite conductive nanoparticles is known as a nanofluid. In contrast to larger particles, these nanoparticles are easily suspended in the base fluid for long enough duration. The prodigious effort of nanofluid was presented by Choi [1]. Due to the magnificent heat performances, the nanofluid is accepted as a dominant source of energy and has many applications in modern thermal technological and industrial developments. Wen and Ding [2] examined the electrostatic stability processes and the use of a high-shear mixing homogenizer to distribute titanium nanoparticles in pure water. In order to investigate the performance of nanofluids in terms of thermal transference under the conditions of natural convection, these nanofluids are discovered to be extremely stable. Lin and Ghaffari [3] explored heat transmission phenomena of power-law fluid within two extending disks separated by a fixed distance and rotate coaxially. They discovered that rotation improves the velocity components. Wang *et al.* [4] summarized the fundamental ideas of slip conditions including their definition and categories. An analysis was conducted by Tyler *et al.* [5] to determine how nanoparticles, specifically nanodiamonds, affect heat transfer in fluids and polymer solids. Techniques are discussed for dispersing nanoparticles in liquids and solids. Heat transfer properties of liquid suspensions are qualitatively compared using a custom thermal transport test setup that measures particle size distributions and fluid viscosities. Using a flash lamp technique, the thermal conductivity of polymer samples is measured to ensure nanoparticle dispersion. A hybrid nanofluid is another creation with enhanced thermal properties than traditional base fluids and nanofluids. Nanoparticles are mixed into a base fluid to form this mixture. In the composition of nanofluids or hybrid nanofluids, metal carbide, metal nitride, metals, metal oxides, and other carbon-based compounds are the most often employed nanoparticles. Sajid and Ali [6] presented an inclusive review of the hybrid nanofluids' thermal conductivity by overviewing the theoretical and experimental studies on the hybrid nanofluids. They discussed various dynamics affecting thermal conductivity, including nanoparticle type, temperature, variability of pH, and sonication time. The hybrid nanofluid slip flow was inspected by Wahid *et al.* [7] over a permeable sheet that was stretching/shrinking exponentially over time. The application of alumina and copper in a hybrid system using H_2O as base fluid is examined and proved that volume fractions on copper nanoparticles can increase both the dragging force and Nusselt number. Yasir and Khan [8] addressed the blood-based hybrid nanofluid flow containing Cu and Ag nanoparticles past a stretching surface using porous media. Their results show that the hybrid nanofluid flow has better performance in terms of heat transfer when compared to blood fluid. Babu *et al.* [9] investigated the slip flow of a nanofluid past a nonlinear stretching surface. They observed that the rate of heat transfer is higher on the nonlinear stretching surface when compared to linear stretching surface. Yasir *et al.* [10] presented the stability analysis of a hybrid nanofluid flow over a shrinking/stretching curved surface with nonlinear thermal radiation and heat source and found that the rate of heat transfer increases with the higher thermal radiation factor. Kumaraswamy Naidu *et al.* [11] examined the sodium alginate-based nanofluid flow containing Fe_3O_4 nanoparticles over a thermally convective extending surface. They found that the higher thermal Biot number heightens the rate of heat transfer. Harish Babu and Satya Narayana [12] investigated the Jeffrey nanofluid flow due to rotating stretching surface. Yasir *et al.* [13] addressed the heat transfer analysis of hybrid nanofluid flows over a stretching/shrinking surface. They found that the skin friction increases and velocity distribution reduces with the higher magnetic factor. Some other relevant studies can be seen in refs [14–16].

In order to illustrate the impression of Brownian motion and thermophoretic diffusion, different investigators have used the prominent Buongiorno model. Pakravan and Yaghoubi [17] considered the nanoparticle passage of a

natural convective thermal transfer of nanofluids. Sheikholeslami and Ganji [18] investigated the heat transmission characteristics of a three-dimensional flow on a rotating sheet with the effects of magnetic field, thermophoresis, and Brownian motion factors. They observed that the magnetic and rotating factors have a direct relation with the skin friction. Also, the Reynolds number has a similar relation with the Nusselt number. Goudarzi *et al.* [19] addressed the Brownian motion of the water-based hybrid nanofluid comprising Ag and MgO nanoparticles in an enclosure. They showed that there is 11% increment in Nusselt number due to the increasing thermophoresis diffusion of both Ag and MgO nanoparticles. Abdelmalek *et al.* [20] discussed the bioconvection magnetohydrodynamics nanofluid flow over an extending sheet with the features of thermal absorption/generation and activation energy by considering the velocity slips and convective conditions. Abdelmalek *et al.* [21] analyzed the 3D flow of cross-liquid with chemical reaction. Dawar *et al.* [22] examined hybrid nanofluid flow on a convectively heated curved surface with variable internal heating and Brownian motion. They found that the hybrid nanofluid case experienced more effects from the embedded factor when compared to the nanofluid case.

The importance of rotating disk induced flows in a variety of real-world applications, including aerospace engineering, and food processing technologies, rotational air cleaners, centrifugal pumps, rotor-stator systems, gas turbine engineering, chemical industries, chemical engineering, and turbomachinery. A steady rotating flow of liquid close to a spinning disk was proposed by Kármán [23]. An approximate integral approach was used in the study by Kármán [23] to obtain analytical solutions. Miklavčič [24] identified a few errors in Von Kármán analysis and produced precise numerical estimates for the principal equations. Stuart [25] investigated the Von Kármán flow over a revolving disk of infinite radius with uniform suction and found that the radial component of the flow decreases with the increasing suction factor. Ackroyd [26] studied the laminar flow of fluid past a gyrating disc with suction and injection cases by using series solution with exponents as negative. This method is proven to consistently yield highly accurate solutions for all suction scenarios and for low injection values at the disk surface, demonstrating excellent precision. Shah *et al.* [27] examined fluid flow on a rotating disk with Hall current. Alreshidi *et al.* [28] deliberated on the impacts of Brownian motion and thermophoresis on magnetized nanofluid flow with Joule heating and slip conditions due to porous spinning disk. Jyothi *et al.* [29] considered the effect of activated energy on fluid flow over a revolving disk. Qayyum *et al.* [30] examined the heat transmission of a dissipative flow of fluid amid two revolving disks. Later on, numerous studies [31–39] have been conducted by researchers to investigate different types of flow by considering different physical conditions.

Nanometer-sized metal particles or non-metals and metalloids form the alloy. There are many different types of alloys, but the best ones are brass, steel, phosphor bronze, solder, and gold. In addition to their use in biomedicine, alloys are employed in a wide range of engineering uses like advanced powder technology, fuel cells, surgical implantation, aerospace science technology, drug delivery systems, hip joint replacement processes, nuclear reactors, and various biological treatments. For corrosion protection, nanoparticle coatings of aluminum (AA7075) and titanium (Ti_6Al_4V) alloy nanoparticles are applied to chemical processing equipment, transpiration cooling, wire, fiber, and heat exchangers. Due to the high susceptibility of metallic alloy nanoparticles to magnetic fields, interactions of flows with magnetic fields can alter the physical as well as thermal features of nanofluids, thereby regulating their flow and thermal transference. Hybrid nanofluids, combining titanium alloy and aluminum alloy nanoparticles, offer intriguing possibilities, especially in applications involving rotating disk surfaces. These applications include heat transfer enhancement, tribological applications, cooling systems in electronics, energy conversion systems, material processing and manufacturing, aerospace and automotive applications, and thermal management in renewable energy systems. Being inspired by the above applications of alloys, the authors are interested in investigating the alloys of aluminum (AA7075) and titanium (Ti_6Al_4V) over a rotating disk surface. To make novel this study, the following questions, which are not yet addressed, are to be addressed in the present investigation:

- In which scenario (stretching or shrinking), do the radial and azimuthal velocities exhibit higher values?
- In which scenario (stretching or shrinking), a magnetic field has diverse impact on the Azimuthal velocity, radial velocity, and drag force at the surface of the rotating disk?
- In which case (*i.e.*, linear or nonlinear), the thermal radiation has maximum impact on the temperature of the nanofluids flow?

Which water-based nanofluid flow (*i.e.*, Ti_6Al_4V nanofluid or AA7075 nanofluid) is greatly influenced by the embedded factors?

Thus, to address the above research questions, the authors have taken the water-based nanofluids flow over an angularly rotating disk surface. Two types of alloys called aluminum alloy and titanium alloy are mixed with water to form the water-based nanofluids flow. Initially, a mathematical framework was proposed in the form of

PDEs as presented in Section 2. The numerical solution of the mathematical design is done by using bvp4c MATLAB scheme, which is shown in Section 3. The authentication of the current flow problem and discussion of results are presented in Section 4. The final remarks are concluded in Section 5.

2 Model formulation

Consider a laminar flow of a viscous nanofluid on a rotating disk. The angular velocity of the disk surface is denoted by Ω, which rotates along z-axis. The components of velocity (u, v, w) are analyzed, respectively, in r-, φ-, and z-directions. The flow is influenced by the strength of the magnetic field B_0, which is normal to the flow direction. The rotating disk stretches along a radial direction with velocity $u(r, 0) = \mathrm{Su_w}$, where $u_w = ar$ is the stretching velocity, $S > 0$ denotes the stretching scenario, and $S < 0$ denotes the contracting scenario. In addition, the disk rotates with velocity $v(r, 0) = v_w$ (in anticlockwise direction) with velocity $v_w = r\Omega$ such that $\Omega \geq 0$. C_w, C_f, and C_∞ denote the surface, fluid, and free-stream concentrations, respectively. In addition, T_w, T_f, and T_∞ depict the surface, fluid, and free-stream temperatures, respectively. A geometrical representation is shown in Figure 1. Moreover, the flow assumptions are as follows:

1) Thermophoresis and Brownian motion
2) Chemical reaction and activation energy
3) Viscous dissipation
4) Nonlinear thermal radiation
5) Joule heating
6) Convective conditions

Thus, the leading equations are defined as follows [38,40,41]:

$$\frac{\partial u}{\partial r} + \frac{u}{r} + \frac{\partial w}{\partial z} = 0, \tag{1}$$

$$\rho_{\mathrm{nf}}\left(w\frac{\partial u}{\partial z} - \frac{v^2}{r} + u\frac{\partial u}{\partial r}\right) = -\frac{\partial p}{\partial r} + \mu_{\mathrm{nf}}\left(\frac{\partial^2 u}{\partial r^2} + \frac{\partial^2 u}{\partial z^2} + \frac{1}{r}\frac{\partial u}{\partial r} - \frac{u}{r^2}\right) - \sigma_{\mathrm{nf}}B_0^2 u, \tag{2}$$

$$\rho_{\mathrm{nf}}\left(u\frac{\partial v}{\partial r} + w\frac{\partial v}{\partial z} + \frac{uv}{r}\right) = \mu_{\mathrm{nf}}\left(\frac{\partial^2 v}{\partial r^2} + \frac{\partial^2 v}{\partial z^2} - \frac{v}{r^2} + \frac{1}{r}\frac{\partial u}{\partial r}\right) - \sigma_{\mathrm{nf}}B_0^2 v, \tag{3}$$

$$\rho_{\mathrm{nf}}\left(w\frac{\partial w}{\partial z} + u\frac{\partial w}{\partial r}\right) = -\frac{\partial p}{\partial z} + \mu_{\mathrm{nf}}\left(\frac{\partial^2 w}{\partial r^2} + \frac{\partial w}{\partial r}\frac{1}{r} + \frac{\partial^2 w}{\partial z^2}\right), \tag{4}$$

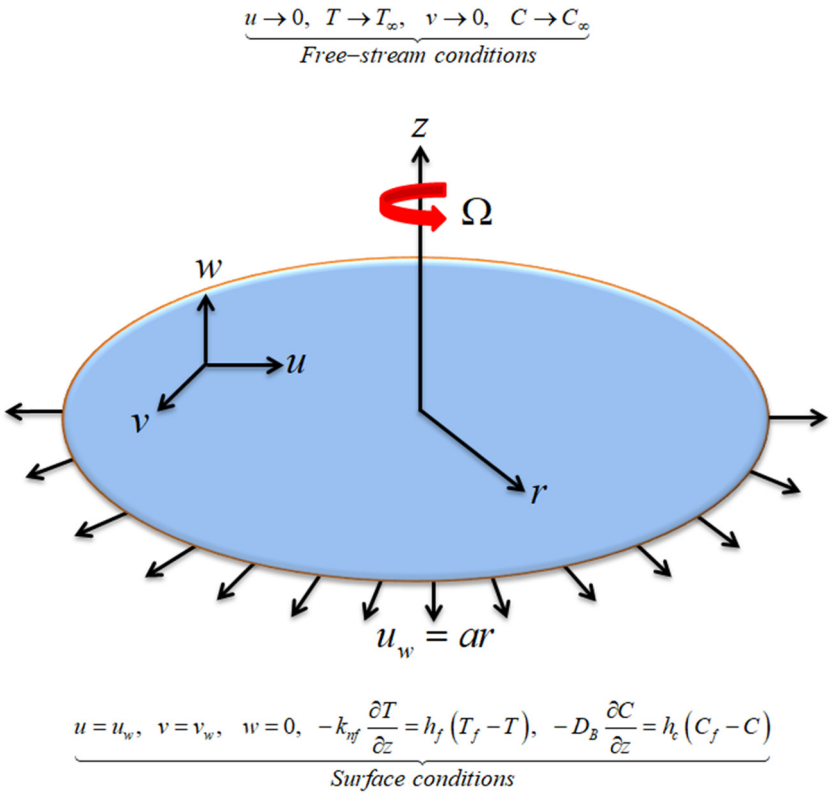

Figure 1: Flow geometry of the problem.

$$
\begin{aligned}
&(\rho C_{\mathrm{p}})_{\mathrm{nf}}\left(u\frac{\partial T}{\partial r}+w\frac{\partial T}{\partial z}\right)\\
&\quad=k_{\mathrm{nf}}\left(\frac{\partial^2 T}{\partial r^2}+\frac{\partial^2 T}{\partial z^2}+\frac{1}{r}\frac{\partial T}{\partial r}\right)+\frac{16\sigma^* T_\infty^3}{3k^*}\left(T\frac{\partial^2 T}{\partial z^2}\right.\\
&\qquad\left.+3\left(\frac{\partial T}{\partial z}\right)^2\right)+(\rho C_{\mathrm{p}})_{\mathrm{np}}\left(D_{\mathrm{B}}\left(\frac{\partial C}{\partial r}\frac{\partial T}{\partial r}+\frac{\partial C}{\partial z}\frac{\partial T}{\partial z}\right)\right.\\
&\qquad\left.+\frac{D_{\mathrm{T}}}{T_\infty}\left(\left(\frac{\partial T}{\partial z}\right)^2+\left(\frac{\partial T}{\partial r}\right)^2\right)\right)+\sigma_{\mathrm{nf}}B_0^2(u^2+v^2)\\
&\qquad+\mu_{\mathrm{nf}}\left(\frac{\partial u}{\partial z}+\frac{\partial v}{\partial z}\right),
\end{aligned}
\tag{5}
$$

$$
\begin{aligned}
u\frac{\partial C}{\partial r}+w\frac{\partial C}{\partial z}&=D_{\mathrm{B}}\left(\frac{1}{r}\frac{\partial C}{\partial r}+\frac{\partial^2 C}{\partial r^2}+\frac{\partial^2 C}{\partial z^2}\right)\\
&\quad+\frac{D_{\mathrm{T}}}{T_\infty}\left(\frac{\partial T}{\partial r}\frac{1}{r}+\frac{\partial^2 T}{\partial r^2}+\frac{\partial^2 T}{\partial z^2}\right)\\
&\quad-k_r\left(\frac{T}{T_\infty}\right)^n e^{\left(-\frac{E_{\mathrm{a}}}{KT}\right)}(C-C_\infty).
\end{aligned}
\tag{6}
$$

The boundary limitations are

$$
\left\{\begin{array}{l}
u=u_{\mathrm{w}},\quad v=v_{\mathrm{w}},\quad w=0,\quad -k_{\mathrm{nf}}\dfrac{\partial T}{\partial z}=h_{\mathrm{f}}(T_{\mathrm{f}}-T),\\
-D_{\mathrm{B}}\dfrac{\partial C}{\partial z}=h_{\mathrm{c}}(C_{\mathrm{f}}-C)\quad \text{at}\quad z=0,\\
u\to 0,\quad T\to T_\infty,\quad v\to 0,\quad C\to C_\infty\quad \text{as}\quad z\to\infty
\end{array}\right\}.
\tag{7}
$$

The thermophysical features of nanofluid are characterized as follows:

$$
\left\{\begin{array}{l}
\dfrac{\mu_{\mathrm{nf}}}{\mu_{\mathrm{f}}}=\dfrac{1}{(1-\phi)^{2.5}},\quad \rho_{\mathrm{nf}}=\rho_{\mathrm{f}}(1-\phi)+\phi\rho_{\mathrm{np}},\\
(\rho C_{\mathrm{p}})_{\mathrm{nf}}=(\rho C_{\mathrm{p}})_{\mathrm{f}}(1-\phi)+\phi(\rho C_{\mathrm{p}})_{\mathrm{np}},\\
\sigma_{\mathrm{nf}}=\left[\dfrac{\sigma_{\mathrm{np}}+2\sigma_{\mathrm{f}}-2(\sigma_{\mathrm{f}}-\sigma_{\mathrm{np}})\phi}{\sigma_{\mathrm{np}}+2\sigma_{\mathrm{f}}+(\sigma_{\mathrm{f}}-\sigma_{\mathrm{np}})\phi}\right]\sigma_{\mathrm{f}},\\
k_{\mathrm{nf}}=\left[\dfrac{k_{\mathrm{np}}+2k_{\mathrm{f}}-2(k_{\mathrm{f}}-k_{\mathrm{np}})\phi}{k_{\mathrm{np}}+2k_{\mathrm{f}}+(k_{\mathrm{f}}-k_{\mathrm{np}})\phi}\right]k_{\mathrm{f}},
\end{array}\right\}.
\tag{8}
$$

Table 1 shows the thermophysical features of the base fluid and nanoparticles.

Table 1: Thermophysical features of the base fluid and nanoparticles [42,43]

Properties	H_2O	AA7075	Ti_6Al_4V
σ	0.005	26.77×10^6	5.8×10^5
k	0.613	173	7.2
C_{p}	4,179	960	0.56
ρ	997.1	2,810	4,420

The similarity variables are defined as follows [23,40,44]:

$$
\begin{aligned}
&u=\Omega r f(\eta),\quad v=r\Omega h(\eta),\quad w=\sqrt{\Omega\nu_{\mathrm{f}}}\,g(\eta),\\
&\psi(\eta)=\frac{C-C_\infty}{C_{\mathrm{f}}-C_\infty},\quad \theta(\eta)=\frac{T-T_\infty}{T_{\mathrm{f}}-T_\infty},\quad \eta=\sqrt{\frac{\Omega}{\nu_{\mathrm{f}}}}z.
\end{aligned}
\tag{9}
$$

Using Eq. (9) in Eqs. (1)–(7), we have

$$
g'+2f=0,
\tag{10}
$$

$$
\left(\frac{\mu_{\mathrm{nf}}/\mu_{\mathrm{f}}}{\rho_{\mathrm{nf}}/\rho_{\mathrm{f}}}\right)f''+h^2-f^2-gf'-\left(\frac{\sigma_{\mathrm{nf}}/\sigma_{\mathrm{f}}}{\rho_{\mathrm{nf}}/\rho_{\mathrm{f}}}\right)Mf=0,
\tag{11}
$$

$$
\left(\frac{\mu_{\mathrm{nf}}/\mu_{\mathrm{f}}}{\rho_{\mathrm{nf}}/\rho_{\mathrm{f}}}\right)h''-2fh-gh'-\left(\frac{\sigma_{\mathrm{nf}}/\sigma_{\mathrm{f}}}{\rho_{\mathrm{nf}}/\rho_{\mathrm{f}}}\right)Mh=0,
\tag{12}
$$

$$
\begin{aligned}
&\left(\frac{k_{\mathrm{nf}}}{k_{\mathrm{f}}}+\mathrm{Rd}(1+(\theta_{\mathrm{w}}-1)\theta)^3\right)\theta''\\
&\quad+\mathrm{Rd}(\theta_{\mathrm{w}}-1)(1+(\theta_{\mathrm{w}}-1)\theta)^2\theta'^2\\
&\quad+\frac{\sigma_{\mathrm{nf}}}{\sigma_{\mathrm{f}}}M\mathrm{EcPr}(f^2+h^2)+\frac{\mu_{\mathrm{nf}}}{\mu_{\mathrm{f}}}M((f'^2+h'^2))\\
&\quad-\mathrm{Pr}\frac{(\rho C_{\mathrm{p}})_{\mathrm{hnf}}}{(\rho C_{\mathrm{p}})_{\mathrm{f}}}g\theta'+\mathrm{PrNt}\theta'^2+\mathrm{PrNb}\theta'\psi'=0,
\end{aligned}
\tag{13}
$$

$$
\psi''+\frac{\mathrm{Nt}}{\mathrm{Nb}}\theta''-\mathrm{Sc}g\psi'-K_r\mathrm{Sc}(1+\sigma\theta)e^{\left(-\frac{E}{(1+\sigma\theta)}\right)}\psi=0,
\tag{14}
$$

$$
\left\{\begin{array}{l}
f(0)=S,\quad h(0)=1,\quad g(0)=0,\\
\dfrac{k_{\mathrm{nf}}}{k_{\mathrm{f}}}\theta'(0)=-\mathrm{Bi_T}(1-\theta(0)),\quad \psi'(0)=-\mathrm{Bi_C}(1-\psi(0)),\\
f(\infty)=0,\quad h(\infty)=0,\quad \theta(\infty)=0,\quad \psi(\infty)=0.
\end{array}\right\}
\tag{15}
$$

The main factors are described as follows:

$$
\left\{\begin{array}{l}
M=\dfrac{\sigma_{\mathrm{f}}B_0^2}{\rho_{\mathrm{f}}\Omega},\quad \mathrm{Pr}=\dfrac{\nu_{\mathrm{f}}(\rho C_{\mathrm{p}})_{\mathrm{f}}}{k_{\mathrm{f}}},\quad \omega=\dfrac{T_{\mathrm{f}}-T_\infty}{T_\infty},\\
\mathrm{Bi_T}=\dfrac{h_{\mathrm{f}}}{k_{\mathrm{f}}}\sqrt{\dfrac{\nu_{\mathrm{f}}}{\Omega}},\quad \mathrm{Rd}=\dfrac{16\sigma^* T_\infty^3}{3k^* k_f},\quad K_r=\dfrac{k_{\mathrm{r}}}{\Omega},\\
\mathrm{Sc}=\dfrac{\nu_{\mathrm{f}}}{D_{\mathrm{B}}},\mathrm{Nt}=\dfrac{(\rho C_{\mathrm{p}})_{\mathrm{np}}D_{\mathrm{T}}(T_{\mathrm{f}}-T_\infty)}{(\rho C_{\mathrm{p}})_{\mathrm{f}}T_\infty\nu_{\mathrm{f}}},\\
\mathrm{Nb}=\dfrac{(\rho C_{\mathrm{p}})_{\mathrm{np}}D_{\mathrm{B}}(C_{\mathrm{w}}-C_\infty)}{(\rho C_{\mathrm{p}})_{\mathrm{f}}\nu_{\mathrm{f}}},\quad \mathrm{Bi_C}=\dfrac{h_{\mathrm{m}}}{D_{\mathrm{B}}}\sqrt{\dfrac{\nu_{\mathrm{f}}}{\Omega}},\\
E=\dfrac{E_{\mathrm{a}}}{KT_\infty},\quad \theta_{\mathrm{w}}=\dfrac{T_{\mathrm{f}}}{T_\infty},
\end{array}\right\}.
\tag{16}
$$

Skin friction coefficient and Nusselt and Sherwood numbers are described mathematically as follows [45]:

$$
\begin{aligned}
&C_{\mathrm{fr}}=\frac{\sqrt{\tau_{\mathrm{wr}}^2+\tau_{\mathrm{wz}}^2}}{\rho_{\mathrm{f}}(\Omega r)^2},\quad \mathrm{Nu_r}=\frac{rq_{\mathrm{w}}}{k_{\mathrm{f}}(T_{\mathrm{f}}-T_\infty)},\\
&\mathrm{Sh_r}=\frac{rq_{\mathrm{m}}}{D_{\mathrm{B}}(C_{\mathrm{f}}-C_\infty)},
\end{aligned}
\tag{17}
$$

where

$$\tau_{wr} = \mu_{nf}\left(\frac{\partial u}{\partial z} + \frac{\partial w}{\partial r}\right)\Big|_{z=0},$$
$$\tau_{wz} = \mu_{nf}\left(\left(\frac{1}{r}\right)\frac{\partial w}{\partial \varphi} + \frac{\partial v}{\partial z}\right)\Big|_{z=0}, \quad (18)$$
$$q_w = -rk_f\left(1 + \frac{16\sigma^*}{3k^*k_f}\right)\frac{\partial T}{\partial z}\Big|_{z=0}, \quad q_m = -rD_B\frac{\partial C}{\partial z}\Big|_{z=0}.$$

Thus, the above equation is reduced as follows:

$$\sqrt{\mathrm{Re}_r}C_f = \frac{\mu_{nf}}{\mu_f}\sqrt{f'^2(0) + h'^2(0)},$$
$$\frac{1}{\sqrt{\mathrm{Re}_r}}\mathrm{Nu} = -\left(\frac{k_{nf}}{k_f} + \mathrm{Rd}(1 + (\theta_w - 1)\theta(0))^3\right)\theta'(0), \quad (19)$$
$$\frac{1}{\sqrt{\mathrm{Re}_r}}\mathrm{Sh} = -\psi'(0),$$

$$\xi'(1) = -2\xi(2), \quad (21)$$

$$\xi'(3) = -\left\{\frac{(\xi(4))^2 - (\xi(3))^2 - \xi(1)\xi(3) - \left(\frac{\sigma_{nf}/\sigma_f}{\rho_{nf}/\rho_f}\right)M\xi(2)}{\left(\frac{\mu_{nf}/\mu_f}{\rho_{nf}/\rho_f}\right)}\right\}, \quad (22)$$

$$\xi'(5) = \left\{\frac{-2\xi(2)\xi(4) - \xi(1)\xi(5) - \left(\frac{\sigma_{nf}/\sigma_f}{\rho_{nf}/\rho_f}\right)M\xi(4)}{\left(\frac{\mu_{nf}/\mu_f}{\rho_{nf}/\rho_f}\right)}\right\}, \quad (23)$$

$$\xi'(7) = -\left\{\frac{\begin{array}{l}\mathrm{Rd}(\theta_w - 1)(1 + (\theta_w - 1)\xi(6))^2(\xi(7))^2 + \frac{\sigma_{nf}}{\sigma_f}\mathrm{MEcPr}((\xi(2))^2 + (\xi(4))^2)\\ + \frac{\mu_{nf}}{\mu_f}M(((\xi(3))^2 + (\xi(5))^2)) - \mathrm{Pr}\frac{(\rho C_p)_{hnf}}{(\rho C_p)_f}\xi(5)\xi(7) + \mathrm{PrNt}(\xi(7))^2 + \mathrm{PrNb}\xi(7)\xi(9)\end{array}}{\left(\frac{k_{nf}}{k_f} + \mathrm{Rd}(1 + (\theta_w - 1)\xi(6))^3\right)}\right\}, \quad (24)$$

where $\mathrm{Re}_r\frac{\Omega r^2}{\nu_f}$ is the local Reynolds number.

$$\xi' - \left\{\frac{\mathrm{Nt}}{\mathrm{Nb}}\xi'(7) - \mathrm{Sc}\xi(4)\xi(9) - K_r\mathrm{Sc}(1 + \sigma\xi(6))e^{\left(-\frac{E}{(1+\sigma\xi(6))}\right)}\xi(8)\right\}, \quad (25)$$

3 Numerical solution

The shooting method is used in the current model to carry out the numerical analysis [46–49]. The bvp4c MATLAB scheme is used to investigate the first-order system of equations. This approach has the benefits of solving nonlinear system of equations with small effect, allows us to define the error tolerance on our own, can solve those systems that are challenging by using analytical methods, and provides solutions faster than other methods. To apply this technique, let us assume that

$$\left\{\begin{array}{lll} g = \xi(1), & g' = \xi'(1) & \\ f = \xi(2), & f' = \xi(3), & f'' = \xi'(3) \\ h = \xi(4), & h' = \xi(5), & h'' = \xi'(5) \\ \theta = \xi(6), & \theta' = \xi(7), & \theta'' = \xi'(7) \\ \psi = \xi(8), & \psi' = \xi(9), & \psi'' = \xi'(9) \end{array}\right\}. \quad (20)$$

Then, the modeled ODEs can be written as follows:

$$\left\{\begin{array}{l} \xi_{Initial}(2) = S, \quad \xi_{Initial}(4) = 1, \quad \xi_{Initial}(1) = 0, \\ \frac{k_{nf}}{k_f}\xi_{Initial}(7) = -\mathrm{Bi}_T(1 - \xi_{Initial}(6)), \\ \xi_{Initial}(9) = -\mathrm{Bi}_C(1 - \xi_{Initial}(8)), \quad \xi_{Boundary}(2) = 0, \\ \xi_{Boundary}(4) = 0, \quad \xi_{Boundary}(6) = 0, \quad \xi_{Boundary}(8) = 0 \end{array}\right\} \quad (26)$$

.

4 Discussion of results

In this section, we have presented the physical discussion of the flow profiles. The nanofluids flow (Ti_6Al_4V–H_2O nanofluid and AA7075–H_2O nanofluid) over a disk surface that rotates angularly is considered here. Two important cases, namely the stretching case and the shrinking case, were investigated to analyze the flow behaviors due to the

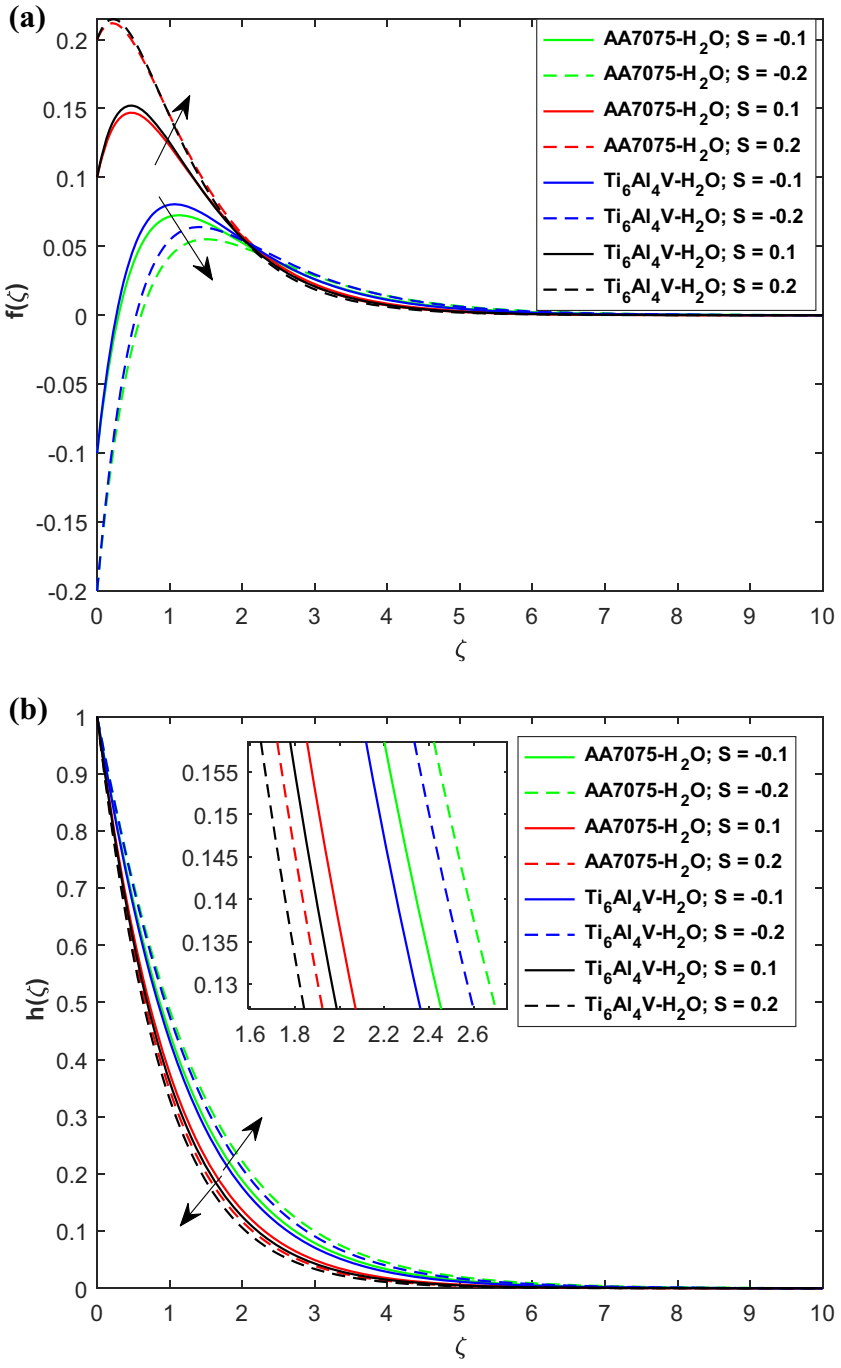

Figure 2: (a) $f(\zeta)$ *vs* S. (b) $h(\zeta)$ *vs* S.

different embedding factors. Figures 2–8 and Tables 3–5 are displayed in this regard. Figure 2(a) displays the impact of stretching/shrinking (S) on radial velocity profile ($f(\zeta)$). Here, the results of S are shown for two different cases of the disk: (i) when the disk stretches ($S > 0$) and (ii) when the disk shrinks ($S < 0$). For $S > 0$, $f(\zeta)$ increases, and for $S < 0$, $f(\zeta)$ reduces. These effects are obvious due to the physical phenomena of the surface. In addition, the effect of S is greater for Ti_6Al_4 V$-H_2O$ nanofluid when compared to AA7075$-H_2O$ nanofluid for both $S > 0$ and $S < 0$. Figure 2(b) displays the impression of stretching/shrinking (S) on Azimuthal velocity profile ($h(\zeta)$). Here, the results of S are shown for two different cases of the disk: (i) when the disk stretches ($S > 0$) and (ii) when the disk shrinks ($S < 0$). For $S < 0$, $h(\zeta)$ increases, and for $S > 0$, $h(\zeta)$ reduces. In addition, it is concluded that when the disk shrinks, $h(\zeta)$ increases, and when the disk stretches, $h(\zeta)$ reduces as shown in Figure 3(a). In addition, AA7075$-H_2O$ nanofluid

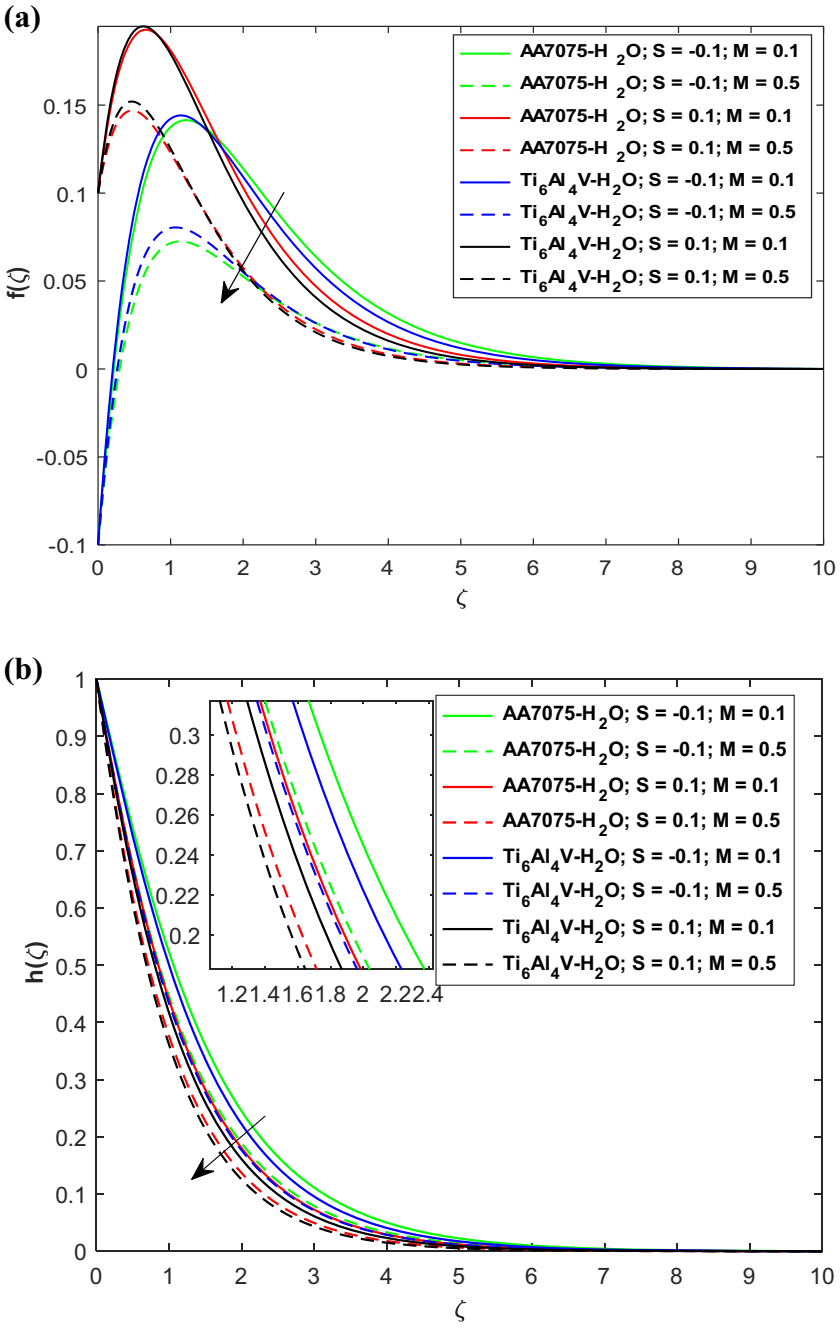

Figure 3: (a) $f(\zeta)$ *vs* M. (b) $h(\zeta)$ *vs* M.

has maximum velocity for both the shrinking and stretching disks when compared to Ti_6Al_4 V−H_2O nanofluid. Figures 3(b) and 4(b) show consequences of magnetic factor (M) on $f(\zeta)$, $h(\zeta)$, and temperature ($\theta(\zeta)$) panels. Both $f(\zeta)$ and $h(\zeta)$ reduce with greater M while $\theta(\zeta)$ reduces. Physically, the greater M produces the contrasting force to the flow because of the Lorentz force. The Lorentz force is impeding force performing in contradiction of the flow particles motion. As we increase M, the greater Lorentz forces produce that declines velocity of fluid. Therefore, both $f(\zeta)$ and $h(\zeta)$ reduce with higher M. In addition, M increases when the disk stretches. Furthermore, this effect is greater for AA7075−H_2O nanofluid when compared to Ti_6Al_4 V−H_2O nanofluid. On the other hand, the greater Lorentz force produces higher thermal transference rate at the surface of disk and results in augmentation of thermal distribution. Therefore, the greater M augments $\theta(\zeta)$. In addition, an important phenomenon is discussed here (linear and nonlinear thermal radiation). $\theta_w = 1$ shows the linear and $\theta_w > 1$ shows the nonlinear thermal radiation. θ_w is ratio of

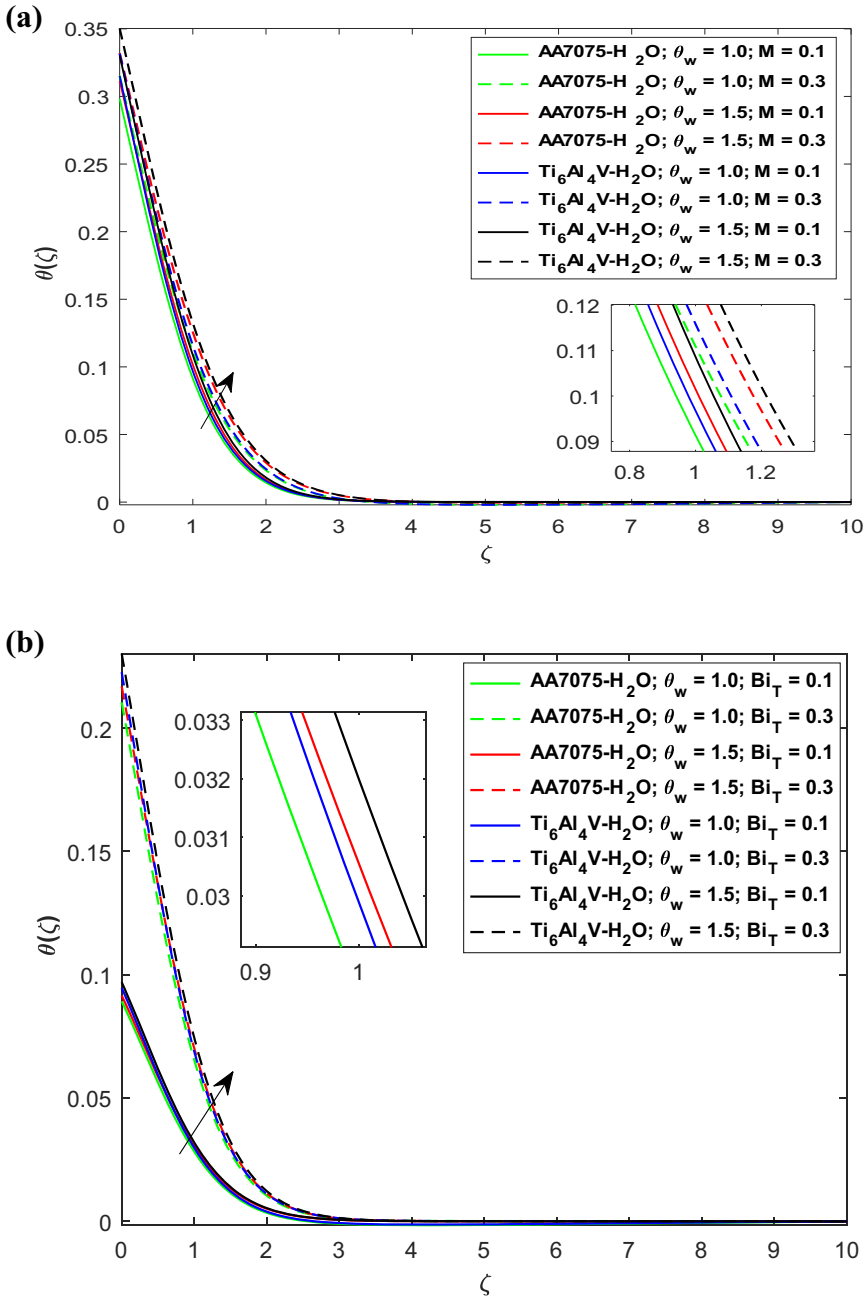

Figure 4: (a) $\theta(\zeta)$ *vs* M. (b) $\theta(\zeta)$ *vs* $\mathrm{Bi_T}$.

reference temperature (T_f) to free-stream temperature (T_∞). So by definition, $\theta_w > 1$ shows the more significance impact than $\theta_w = 1$. This is only possible for reference temperature to be greater than as it is at free-stream. The higher the reference temperature, the greater the heat generated in the flow system. The more heat in the flow system definitely shows the higher temperature. This phenomenon is shown Figure 5(a). Figure 5(b) expresses the impression of thermal Biot number ($\mathrm{Bi_T}$) on $\theta(\zeta)$. The results show that the increasing $\mathrm{Bi_T}$ increases $\theta(\zeta)$. Actually, the increasing $\mathrm{Bi_T}$ increases the coefficient of heat transfer. The increasing coefficient of heat transfer has direct relation with $\mathrm{Bi_T}$. So by this fact, the increasing $\mathrm{Bi_T}$ heightens the thermal transference rate, which consequently increases the temperature distribution. In addition, the impression of $\mathrm{Bi_T}$ is maximum for the nonlinear thermal radiation case. Also, the higher impact of $\mathrm{Bi_T}$ is perceived for $\mathrm{Ti_6Al_4\ V{-}H_2O}$ nanofluid when compared to $\mathrm{AA7075{-}H_2O}$ nanofluid. Figure 6(a) shows the impact of activation energy parameter (E) on concentration distribution ($\psi(\zeta)$). The higher E heightens the concentration boundary

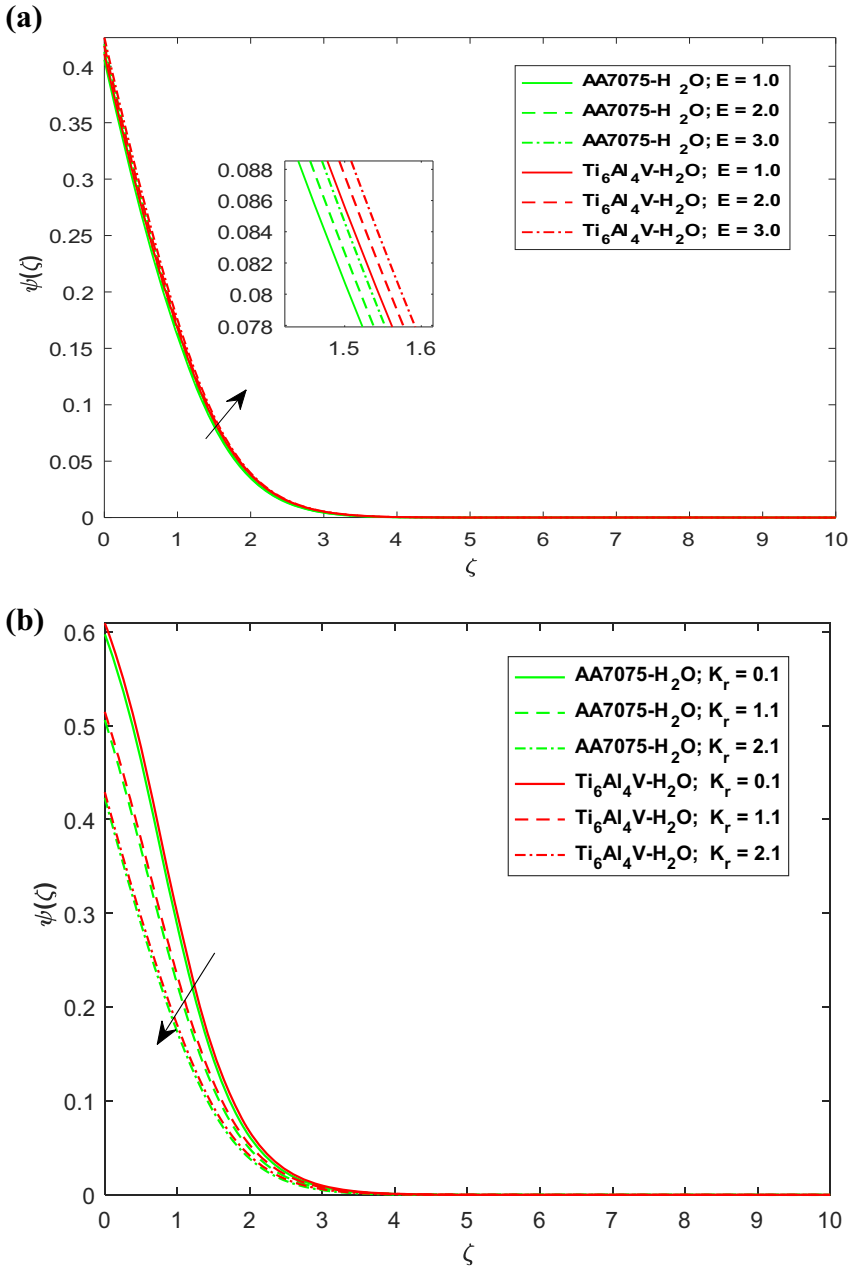

Figure 5: (a) $\psi(\zeta)$ *vs* E. (b) $\psi(\zeta)$ *vs* K_r.

layers, which results in an augmenting impact on $\psi(\zeta)$. In addition, the greater impact is found for Ti_6Al_4 V−H_2O nanofluid when compared to AA7075−H_2O nanofluid. Figure 6(b) expresses the result of chemical reactivity factor (K_r) on $\psi(\zeta)$. The increasing K_r reduces $\psi(\zeta)$. Actually, the increasing K_r diminishes the molecular diffusivity of the nanofluids flow, which results in reduction in the concentration layers at boundary. Therefore, the increasing K_r declines $\psi(\zeta)$. In addition, the greater impact of K_r is observed for Ti_6Al_4 V−H_2O nanofluid when compared to AA7075−H_2O nanofluid. Figure 6(a) exhibits the result of Sc on $\psi(\zeta)$. The higher Sc reduces $\psi(\zeta)$. This is due to the reason that the escalating Sc diminishes the molecular diffusivities of the nanofluids flow, which affects the solutal boundary layer thicknesses to decreases. The reduction in the thicknesses of the boundary layers results in a declining impact of the concentration distribution. Therefore, the higher Sc reduces $\psi(\zeta)$. When compared the two different nanofluids, the maximum impact is found for Ti_6Al_4 V−H_2O nanofluid than AA7075−H_2O nanofluid. Figure 7(a) expresses the impression of concentration Biot number (Bi_C) on $\psi(\zeta)$. The results show that the increasing Bi_C increases $\psi(\zeta)$. The reason is that the

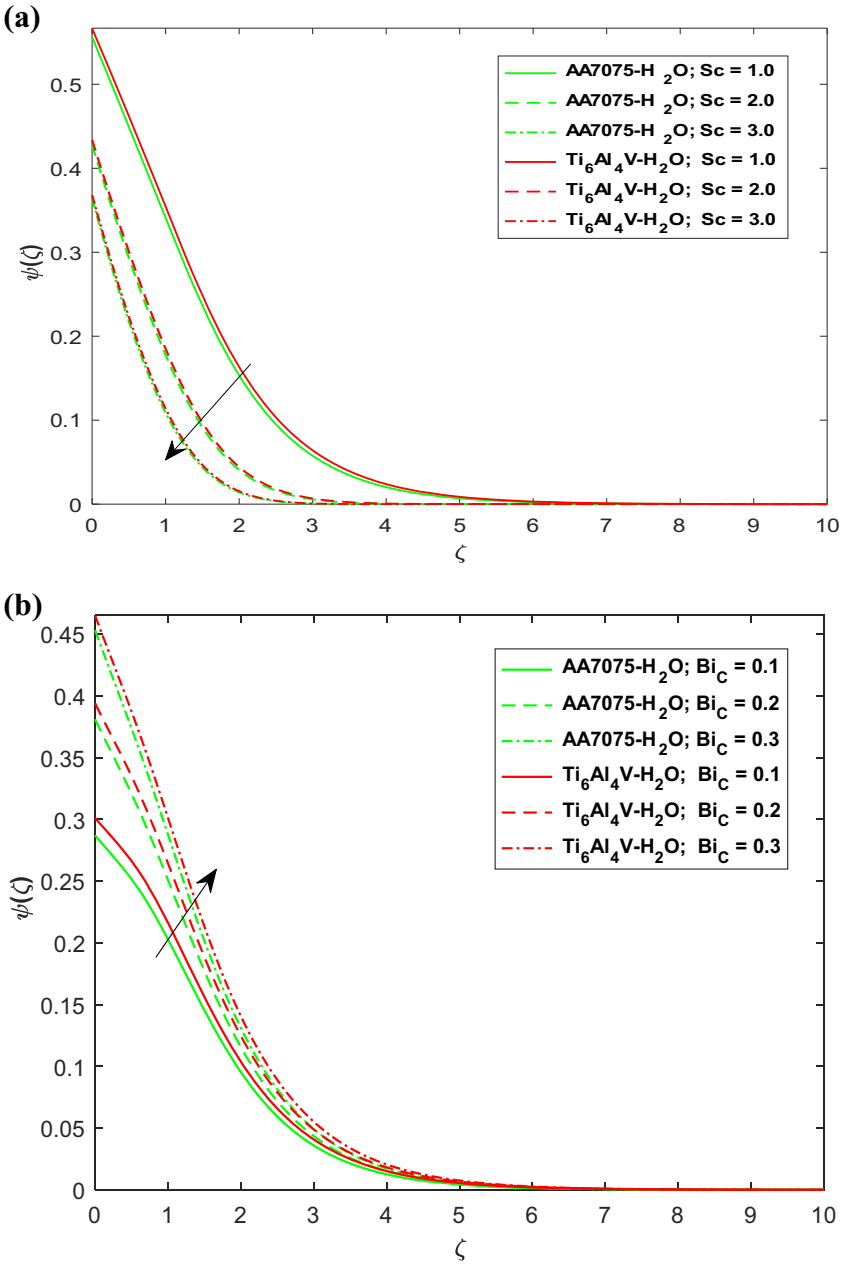

Figure 6: (a) $\psi(\zeta)$ *vs* Sc. (b) $\psi(\zeta)$ *vs* $\mathrm{Bi_C}$.

increasing $\mathrm{Bi_C}$ increases the coefficient of mass transfer. The increasing coefficient of mass transfer has direct relation with $\mathrm{Bi_C}$. So by this fact, the increasing $\mathrm{Bi_C}$ heightens the mass transfer rate and boundary layer of the concentration profile, which consequently increases the concentration distribution. In addition, the higher impact of $\mathrm{Bi_C}$ is perceived for $\mathrm{Ti_6Al_4\ V{-}H_2O}$ nanofluid when compared to $\mathrm{AA7075{-}H_2O}$ nanofluid. Figures 7(b) and 8(a) show the impact of Nt on $\theta(\zeta)$ and $\psi(\zeta)$, respectively. The higher Nt augments both $\theta(\zeta)$ and $\psi(\zeta)$. Actually, the higher Nt strengthens the thermophoretic force, which forces the particles of the nanofluids to move toward the hot region from colder one. This movement of the nanofluid particles enhances the thermal boundary layer and temperature of the nanofluids. Thus, the growing Nt heightens $\theta(\zeta)$. In addition, the impression of Nt is maximum for the nonlinear thermal radiation case. Also, the higher impact of Nt is perceived for $\mathrm{Ti_6Al_4\ V{-}H_2O}$ nanofluid when compared to $\mathrm{AA7075{-}H_2O}$ nanofluid. On the other hand, the concentration boundary layer thicknesses also enhance with increasing Nt, which results in an enhanced impact on the concentration distribution, as shown in Figure 8(b). In addition, the higher impact of Nt is perceived for

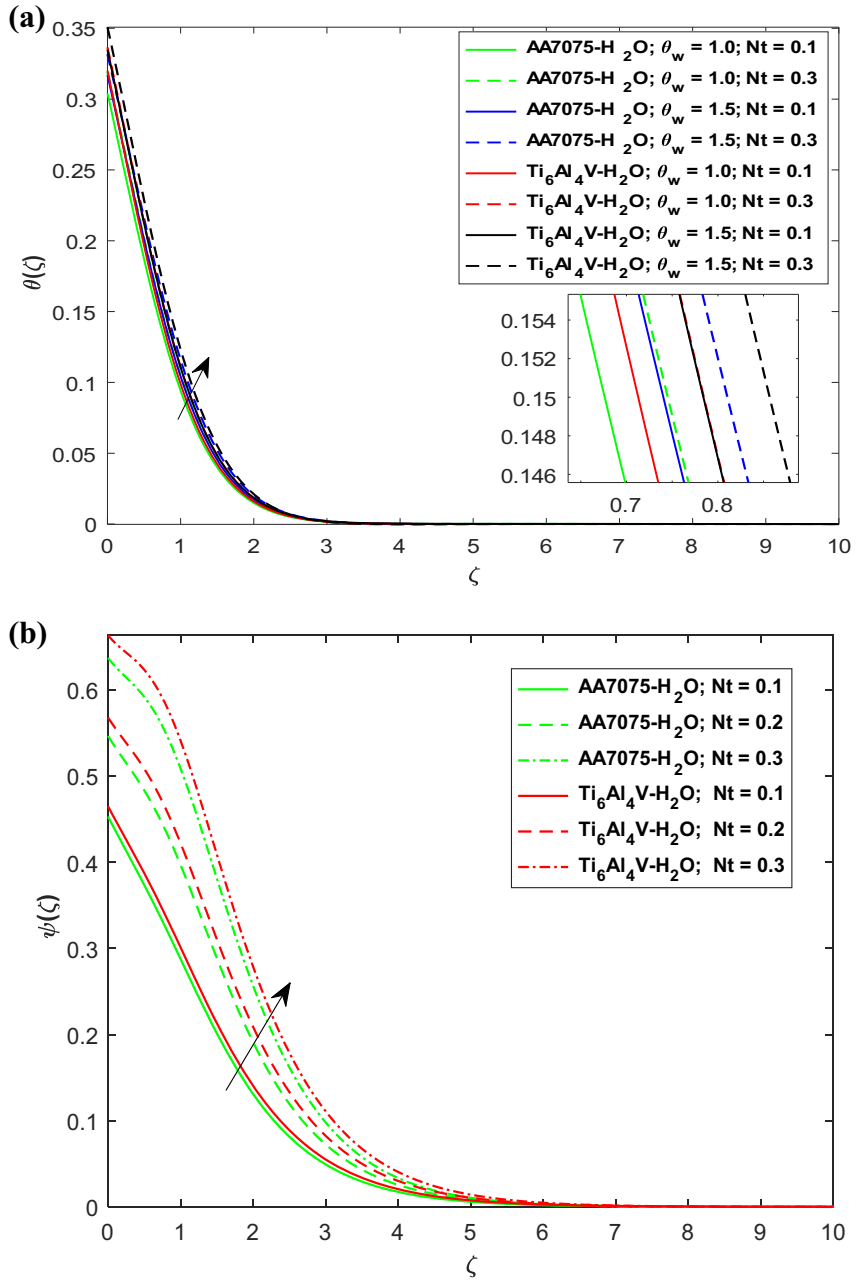

Figure 7: (a) $\theta(\zeta)$ *vs* Nt. (b) $\psi(\zeta)$ *vs* Nt.

Ti_6Al_4 V$-H_2O$ nanofluid when compared to AA7075$-H_2O$ nanofluid. Figure 8(a) and (b) shows the impact of Nb on $\theta(\zeta)$ and $\psi(\zeta)$, respectively. From these figures, we see that the increasing Nb increases $\theta(\zeta)$ but reduces $\psi(\zeta)$. The fact is that the higher Nb increases Brownian motion of the nanofluids particles, which leads to an increase in the temperature and the thermal boundary layers, resulting in augmenting behavior in $\theta(\zeta)$. Furthermore, the impact of Nb is maximum for the nonlinear thermal radiation case. Also, the higher impact of Nb is perceived for Ti_6Al_4 V$-H_2O$ nanofluid when compared to AA7075$-H_2O$ nanofluid. On the other hand, the increasing Nb reduces the mass transfer rate and so are the concentration boundary layers. Thus, the higher Nb reduces $\psi(\zeta)$. In addition, the greater effect of Nb is perceived for Ti_6Al_4 V$-H_2O$ nanofluid when compared to AA7075$-H_2O$ nanofluid. Table 2 expresses the assessment of current analysis with published results of the previous studies. Here, close relations between the present and published results are found, which validate the present analysis. Table 3 displays the impressions of M and S on $\sqrt{\mathrm{Re}_r}C_f$. The higher magnetic factor augments $\sqrt{\mathrm{Re}_r}C_f$. The reason is that the higher M

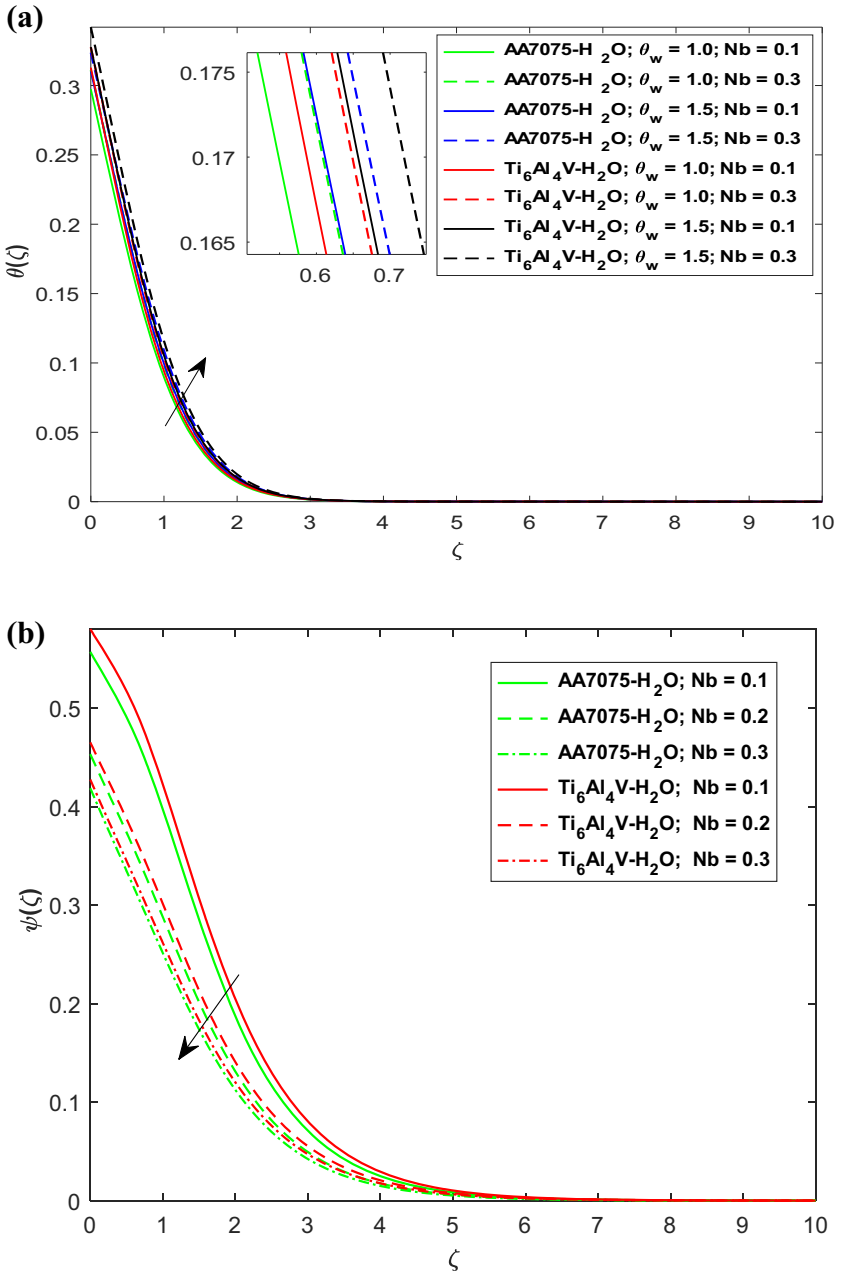

Figure 8: (a) $\theta(\zeta)$ *vs* Nb. (b) $\psi(\zeta)$ *vs* Nb.

Table 2: Validation of the present results with previous studies when $\mathrm{Pr} = 6.2,\ S = 0.0,$ and $\phi = 0.0$

Outcomes	$f'(0)$	$-h'(0)$	$-g(0)$	$-\theta'(0)$
Present	$51.03537103 \times 10^{-2}$	$61.58881969 \times 10^{-2}$	0.8882966310	$93.38779486 \times 10^{-2}$
Kelson and Desseaux [50]	51.0233×10^{-2}	61.5922×10^{-2}	88.4474×10^{-2}	—
Bachok *et al.* [34]	51.02×10^{-2}	61.59×10^{-2}	—	93.37×10^{-2}
Turkyilmazoglu [51]	51.023262×10^{-2}	61.592201×10^{-2}	88.447411×10^{-2}	93.387794×10^{-2}
Abbas *et al.* [52]	50.9175×10^{-2}	61.5375×10^{-2}	88.2042×10^{-2}	93.1855×10^{-2}

Table 3: Impacts of M and S on $\sqrt{\mathrm{Re_r}}C_\mathrm{f}$

M	S	AA7075–H_2O	Ti_6Al_4V–H_2O
1.50	0.1	1.749404207	1.773694765
1.75	0.1	1.863047936	1.884131577
2.00	0.1	1.971631862	1.990188495
1.50	−0.1	1.637009762	1.649974856
1.75	−0.1	1.755704601	1.765142631
2.00	−0.1	1.869070098	1.875921695
1.75	0.1	1.863047936	1.884131577
1.75	0.2	1.943502204	1.970664495
1.75	0.3	2.042922023	2.076507283
1.75	−0.1	1.755704601	1.765142630
1.75	−0.2	1.725669558	1.729275744
1.75	−0.3	1.708472324	1.706096980

enhances the Lorentz force, which always opposes the motion of the fluid particles. Thus, the enhancing Lorentz force increases the drag force at the surface. Therefore, $\sqrt{\mathrm{Re_r}}C_\mathrm{f}$ increases with greater M. In addition, the effect of M on $\sqrt{\mathrm{Re_r}}C_\mathrm{f}$ is higher when $S > 0$. Also, Ti_6Al_4 V−H_2O nanofluid has maximum surface drag than the AA7075−H_2O nanofluid. The impact of S on $\sqrt{\mathrm{Re_r}}C_\mathrm{f}$ is also shown in Table 3. This is obvious that the higher stretching rate will increase the surface drag force, but this effect is opposite for the case of shrinking sheet. Similar impacts are perceived here. In addition, Ti_6Al_4 V−H_2O nanofluid has maximum surface drag than the AA7075−H_2O nanofluid. Table 4 show the impacts of Rd, Nb, Nt, and $\mathrm{Bi_T}$ on local Nusselt number ($\frac{1}{\sqrt{\mathrm{Re_r}}}$Nu). It is observed that $\frac{1}{\sqrt{\mathrm{Re_r}}}$Nu increases with higher values of Rd and $\mathrm{Bi_T}$ and reduces with higher values of Nt and Nb. The increasing Rd means that extra heat generates in the flow system, which obviously increases $\frac{1}{\sqrt{\mathrm{Re_r}}}$Nu. Similarly, the increasing $\mathrm{Bi_T}$ increases the coefficient of heat transfer, which results in an increase in the rate of heat transfer. Thus, $\frac{1}{\sqrt{\mathrm{Re_r}}}$Nu increases with higher $\mathrm{Bi_T}$. On the other hand, $\frac{1}{\sqrt{\mathrm{Re_r}}}$Nu reduces with higher values of Nt and Nb. This indicates that the distribution of nanoparticles in the flow regime may benefit from the Brownian motion process. Moreover, low Nt and Nb values may contribute to temper the flow regime. In addition, Ti_6Al_4 V−H_2O nanofluid has maximum heat transfer rate than the AA7075−H_2O nanofluid. Table 5 expresses the impression of Sc, Nb, Nt, and $\mathrm{Bi_C}$ on $\frac{1}{\sqrt{\mathrm{Re_r}}}$Sh. It is perceived that the greater values of Sc, Nt, and $\mathrm{Bi_C}$ heightens $\frac{1}{\sqrt{\mathrm{Re_r}}}$Sh, while the greater values of Nb diminishes $\frac{1}{\sqrt{\mathrm{Re_r}}}$Sh. In addition, Ti_6Al_4 V−H_2O nanofluid has maximum mass transfer rate than the AA7075−H_2O nanofluid.

Table 4: Impacts of Rd, Nb, Nt, and $\mathrm{Bi_T}$ on $\frac{1}{\sqrt{\mathrm{Re_r}}}$Nu

Rd	Nb	Nt	$\mathrm{Bi_T}$	AA7075–H_2O	Ti_6Al_4V–H_2O
1.0	0.3	0.3	0.5	0.2939523146	0.3055227847
1.5				0.3884742454	0.4038005311
2.0				0.4793603598	0.4975608549
2.0	0.4			0.4614944500	0.4787616300
	0.6			0.4257151773	0.4411786784
	0.8			0.3900292450	0.4037818812
	0.3	0.2		0.4609330164	0.4777864491
		0.4		0.4239745672	0.4382766749
		0.6		0.3870670571	0.3990251843
		0.6	0.6	0.4129920515	0.4245642843
			0.7	0.4334330116	0.4445941612
			0.8	0.4499411309	0.4607029209

Table 5: Impacts of Sc, Nb, Nt, and $\mathrm{Bi_C}$ on $\frac{1}{\sqrt{\mathrm{Re_r}}}$Sh

Sc	Nb	Nt	$\mathrm{Bi_C}$	AA7075–H_2O	Ti_6Al_4V–H_2O
1.0	0.3	0.3	0.5	0.1440435747	0.1454743799
1.5				0.1695438946	0.1716908589
2.0				0.1912788432	0.1938364811
2.0	0.4			0.1916562020	0.1943887531
	0.6			0.1915873040	0.1945021543
	0.8			0.1911107593	0.1941242023
	0.3	0.2		0.1919489729	0.1939343527
		0.4		0.1986035019	0.1996018768
		0.6		0.2124578424	0.2126565364
		0.6	0.6	0.2278976716	0.2283818719
			0.7	0.2403584756	0.2411006010
			0.8	0.2506248389	0.2515980012

5 Conclusion

The electrically conducting viscous nanofluids flow over an angularly gyrating disk is explored in this investigation. Two different types of nanoparticles, namely titanium alloys (Ti_6Al_4V) and aluminum alloys (AA7075). were investigated, whereas water (H_2O) is used as a base fluid. Two important cases, namely the stretching case and the shrinking case, were investigated to analyze the flow behaviors due to the different embedding factors. The impacts of viscous Joule heating, thermophoresis, nonlinear thermal radiation, Brownian motion, activation energy, and chemical reaction are investigated here. At the end of this investigation, the following key points are illustrated:

- The radial flow increases when the surface of the disk stretches and reduces when the disk surface shrinks. On the other hand, the Azimuthal velocity increases when

the disk surface shrinks and reduces when the disk surface stretches.
- Both the radial and Azimuthal flows are the diminishing functions of the magnetic factor, whereas temperature is the escalating function of the magnetic factor. In addition, the temperature is more influenced by the magnetic factor in the case of nonlinear thermal radiation.
- Escalation in thermal Biot number, Brownian motion, and thermophoresis factors result in a rising thermal panel. Furthermore, in a nonlinear thermal radiation scenario, the magnetic factor has a greater influence on temperature.
- High concentration Biot number, activation energy, and thermophoresis factors heighten concentration panels, while high, Brownian motion, Schmidt number, and chemical reactivity factors reduce them.
- Skin friction is increased by a higher magnetic factor. In addition, the higher surface drag is experienced in the elongating scenario in comparison to the contracting scenario.
- The local Nusselt number is an escalating function of thermal radiation and thermal Biot number.
- It is found that the nanofluid flow containing titanium alloys has perceived the greater impacts of the embedded factors when compared to the nanofluid flow containing aluminum alloys.

6 Future recommendations

The existing problem can be modified by using mass flux and zero mass flux conditions to investigate the rate of mass transfer at the surface of the rotating disk. The same model can be extended for hybrid nanofluid flow containing titanium and aluminum alloys by using different types of regular fluids.

Acknowledgments: This work was supported by the Deanship of Scientific Research, the Vice Presidency for Graduate Studies and Scientific Research, King Faisal University, Saudi Arabia (Grant No. 5532).

Funding information: This work was supported by the Deanship of Scientific Research, the Vice Presidency for Graduate Studies and Scientific Research, King Faisal University, Saudi Arabia (Grant No. 5532).

Author contributions: All authors have accepted responsibility for the entire content of this manuscript and approved its submission.

Conflict of interest: The authors state no conflict of interest.

Data availability statement: The datasets generated and/or analyzed during the current study are available from the corresponding author on reasonable request.

References

[1] Choi SUS. Nanofluids: from vision to reality through research. J Heat Transf. 2009;131:033106.
[2] Wen D, Ding Y. Formulation of nanofluids for natural convective heat transfer applications. Int J Heat Fluid Flow. 2005;26:855–64.
[3] Lin P, Ghaffari A. Steady flow and heat transfer of the power-law fluid between two stretchable rotating disks with non-uniform heat source/sink. J Therm Anal Calorim. 2021;146:1735–49.
[4] Wang R, Chai J, Luo B, Liu X, Zhang J, Wu M, et al. A review on slip boundary conditions at the nanoscale: recent development and applications. Beilstein J Nanotechnol. 2021;12:1237–51.
[5] Tyler T, Shenderova O, Cunningham G, Walsh J, Drobnik J, McGuire G. Thermal transport properties of diamond-based nanofluids and nanocomposites. Diam Relat Mater. 2006;15:2078–81.
[6] Sajid MU, Ali HM. Thermal conductivity of hybrid nanofluids: a critical review. Int J Heat Mass Transf. 2018;126:211–34.
[7] Wahid NS, Arifin NM, Khashi'ie NS, Pop I. Hybrid nanofluid slip flow over an exponentially stretching/shrinking permeable sheet with heat generation. Mathematics. 2020;9:30.
[8] Yasir M, Khan M. Comparative analysis for radiative flow of Cu–Ag/blood and Cu/blood nanofluid through porous medium. J Pet Sci Eng. 2022;215:110650.
[9] Babu DH, Reddy SH, Naidu KK, Narayana PVS, Venkateswarlu B. Numerical investigation for entropy-based magneto nanofluid flow over non-linear stretching surface with slip and convective boundary conditions. ZAMM-J Appl Math Mech Für Angew Math Und Mech. 2023;103(10):e202300006.
[10] Yasir M, Khan M, Sarfraz M, Abuzaid D, Ullah MZ. Exploration of the dynamics of ethylene glycol conveying copper and titania nanoparticles on a stretchable/shrinkable curved object: Stability analysis. Int Commun Heat Mass Transf. 2022;137:106225.
[11] Kumaraswamy Naidu K, Harish Babu D, Satya Narayana PV. Bioconvection in magneto hydrodynamics Casson nanoliquid (Fe_3O_4-sodium alginate) with gyrotactic microorganisms over an exponential stretching sheet. J Nanofluids. 2021;10:327–38.
[12] Harish Babu D, Satya Narayana PV. Melting heat transfer and radiation effects on Jeffrey fluid flow over a continuously moving surface with a parallel free stream. J Appl Comput Mech. 2019;5:468–76.
[13] Yasir M, Sarfraz M, Khan M, Alzahrani AK, Ullah MZ. Estimation of dual branch solutions for Homann flow of hybrid nanofluid towards biaxial shrinking surface. J Pet Sci Eng. 2022;218:110990.
[14] Sarfraz M, Khan M, Yasir M. Dynamics of water conveying iron oxide and graphene nanoparticles subject to stretching/spiraling surface: An asymptotic approach. Ain Shams Eng J. 2023;14:102021.

[15] Yasir M, Khan M, Alqahtani AS, Malik MY. Mass transpiration effect on rotating flow of radiative hybrid nanofluid due to shrinking surface with irregular heat source/sink. Case Stud Therm Eng. 2023;44:2214–157. doi: 10.1016/j.csite.2023.102870
[16] Yasir M, Khan M, Alqahtani AS, Malik MY. Numerical study of axi-symmetric hybrid nanofluid MgO-Ag/H2O flow with non-uniform heat source/sink. Alex Eng J. 2023;75:439–6.
[17] Pakravan HA, Yaghoubi M. Analysis of nanoparticles migration on natural convective heat transfer of nanofluids. Int J Therm Sci. 2013;68:79–93. doi: 10.1016/J.IJTHERMALSCI.2012.12.012.
[18] Sheikholeslami M, Ganji DD. Three dimensional heat and mass transfer in a rotating system using nanofluid. Powder Technol. 2014;253:789–96. doi: 10.1016/J.POWTEC.2013.12.042.
[19] Goudarzi S, Shekaramiz M, Omidvar A, Golab E, Karimipour A, Karimipour A. Nanoparticles migration due to thermophoresis and Brownian motion and its impact on Ag-MgO/Water hybrid nanofluid natural convection. Powder Technol. 2020;375:493–503. doi: 10.1016/j.powtec.2020.07.115.
[20] Abdelmalek Z, Khan SU, Waqas H, Riaz A, Khan IA, Tlili I. A mathematical model for bioconvection flow of Williamson nanofluid over a stretching cylinder featuring variable thermal conductivity, activation energy and second-order slip. J Therm Anal Calorim. 2020;144:205–17. doi: 10.1007/s10973-020-09450-z.
[21] Abdelmalek Z, Mahanthesh B, Md Basir MF, Imtiaz M, Mackolil J, Khan NS, et al. Mixed radiated magneto Casson fluid flow with Arrhenius activation energy and Newtonian heating effects: Flow and sensitivity analysis. Alex Eng J. 2020;59:3991–4011. doi: 10.1016/J.AEJ.2020.07.006.
[22] Dawar A, Said NM, Islam S, Shah Z, Mahmuod SR, Wakif A. A semi-analytical passive strategy to examine a magnetized heterogeneous mixture having sodium alginate liquid with alumina and copper nanomaterials near a convectively heated surface of a stretching curved geometry. Int Commun Heat Mass Transf. 2022;139:106452.
[23] Kármán TV. Über laminare und turbulente Reibung. ZAMM - J Appl Math Mech/Zeitschrift Für Angew Math Und Mech. 1921;1:233–52. doi: 10.1002/ZAMM.19210010401.
[24] Miklavčič M, Wang CY. The flow due to a rough rotating disk. Z Für Angew Math Und Phys ZAMP. 2004;55:235–46.
[25] Stuart JT. On the effects of uniform suction on the steady flow due to a rotating disk. Q J Mech Appl Math. 1954;7:446–57.
[26] Ackroyd JAD. On the steady flow produced by a rotating disc with either surface suction or injection. J Eng Math. 1978;12:207–20.
[27] Shah Z, Gul T, Khan AM, Ali I, Islam S, Husain F. Effects of hall current on steady three dimensional non-newtonian nanofluid in a rotating frame with Brownian motion and thermophoresis effects. J Eng Technol. 2017;6:e296.
[28] Alreshidi NA, Shah Z, Dawar A, Kumam P, Shutaywi M, Watthayu W. Brownian motion and thermophoresis effects on MHD three dimensional nanofluid flow with slip conditions and Joule dissipation due to porous rotating disk. Molecules. 2020;25:729. doi: 10.3390/molecules25030729.
[29] Jyothi AM, Naveen Kumar R, Punith Gowda RJ, Veeranna Y, Prasannakumara BC. Impact of activation energy and gyrotactic microorganisms on flow of Casson hybrid nanofluid over a rotating moving disk. Heat Transf. 2021;50:5380–99.
[30] Qayyum S, Khan MI, Hayat T, Alsaedi A, Tamoor M. Entropy generation in dissipative flow of Williamson fluid between two rotating disks. Int J Heat Mass Transf. 2018;127:933–42.
[31] Bödewadt VUT. Die drehströmung über festem grunde. ZAMM-Journal Appl Math Mech Für Angew Math Und Mech. 1940;20:241–53.
[32] Ariel PD. On computation of MHD flow near a rotating disk. ZAMM-Journal Appl Math Mech Für Angew Math Und Mech Appl Math Mech. 2002;82:235–46.
[33] Attia HA. Steady flow over a rotating disk in porous medium with heat transfer. Nonlinear Anal Model Control. 2009;14:21–6.
[34] Bachok N, Ishak A, Pop I. Flow and heat transfer over a rotating porous disk in a nanofluid. Phys B Condens Matter. 2011;406:1767–72.
[35] Hayat T, Rashid M, Imtiaz M, Alsaedi A. Magnetohydrodynamic (MHD) flow of Cu-water nanofluid due to a rotating disk with partial slip. AIP Adv. 2015;5:67169.
[36] Griffiths PT. Flow of a generalised Newtonian fluid due to a rotating disk. J Nonnewton Fluid Mech. 2015;221:9–17. doi: 10.1016/j.jnnfm.2015.03.008.
[37] Turkyilmazoglu M. Three dimensional MHD stagnation flow due to a stretchable rotating disk. Int J Heat Mass Transf. 2012;55:6959–65.
[38] Turkyilmazoglu M. MHD fluid flow and heat transfer due to a stretching rotating disk. Int J Therm Sci. 2012;51:195–201.
[39] Mustafa M, Khan JA, Hayat T, Alsaedi A. On Bödewadt flow and heat transfer of nanofluids over a stretching stationary disk. J Mol Liq. 2015;211:119–25.
[40] Khan U, Bilal S, Zaib A, Makinde OD, Wakif A. Numerical simulation of a nonlinear coupled differential system describing a convective flow of Casson gold–blood nanofluid through a stretched rotating rigid disk in the presence of Lorentz forces and nonlinear thermal radiation. Numer Methods Partial Differ Equ. 2020. doi: 10.1002/NUM.22620.
[41] Mustafa I, Javed T, Ghaffari A. Heat transfer in MHD stagnation point flow of a ferrofluid over a stretchable rotating disk. J Mol Liq. 2016;219:526–32.
[42] Žitňanský M, Čaplovič L. Effect of the thermomechanical treatment on the structure of titanium alloy Ti6Al4V. J Mater Process Technol. 2004;157:643–9.
[43] Jackson MJ, Kopac J, Balazic M, Bombac D, Brojan M, Kosel F. Titanium and titanium alloy applications in medicine. Surg Tools. Med Devices. 2016;475–517.
[44] Ragupathi P, Muhammad T, Islam S, Wakif A. Application of Arrhenius kinetics on MHD radiative Von Kármán Casson nanofluid flow occurring in a Darcy-Forchheimer porous medium in the presence of an adjustable heat source. Phys Scr. 2021;96:125228. doi: 10.1088/1402-4896/AC297C.
[45] Hafeez A, Khan M, Ahmed J. Stagnation point flow of radiative Oldroyd-B nanofluid over a rotating disk. Comput Methods Prog Biomed. 2020;191:105342.
[46] Dawar A, Islam S, Shah Z, Mahmuod SR. A passive control of Casson hybrid nanofluid flow over a curved surface with alumina and copper nanomaterials: A study on sodium alginate-based fluid. J Mol Liq. 2023;382:122018.
[47] Khan I, Rahman AU, Lone SA, Dawar A, Islam S. Numerical investigation of the chemically reactive magnetohydrodynamic blood-gold nanofluid flow between two rotating disks. J Therm Anal Calorim. 2023;148:11903–15.
[48] Ayub A, Sabir Z, Altamirano GC, Sadat R, Ali MR. Characteristics of melting heat transport of blood with time-dependent cross-nanofluid model using Keller–Box and BVP4C method. Eng Comput. 2022;38:3705–19.

[49] Dey D, Chutia B. Two-phase fluid motion through porous medium with volume fraction: An application of MATLAB bvp4c solver technique. Heat Transf. 2022;51:1778–89.
[50] Kelson N, Desseaux A. Note on porous rotating disk flow. ANZIAM J. 2000;42:C837–55.
[51] Turkyilmazoglu M. Nanofluid flow and heat transfer due to a rotating disk. Comput Fluids. 2014;94:139–46. doi: 10.1016/J.COMPFLUID.2014.02.009.
[52] Abbas Z, Naveed M, Tabassum R, Ahmad I. Influence of Hall and Joule heating on a magnetic nanofluid (Fe3O4) flow on a rotating disk with generalized slip condition. Heat Transf. 2021;50:7271–90.